First Results on Terrestrial Gamma-ray Flashes from the Fermi Gamma-ray Burst Monitor

M. S. Briggs,[1] G. J. Fishman,[2] V. Connaughton,[1]
P. N. Bhat,[1] W. S. Paciesas,[1,3] R. D. Preece,[1,3]
C. Wilson-Hodge,[2] V. L. Chaplin,[1] R. M. Kippen,[4]
A. von Kienlin,[5] C. A. Meegan,[6] E. Bissaldi,[5]
J. R. Dwyer,[7] D. M. Smith,[8] R. H. Holzworth,[9]
J. E. Grove,[10] and A. Chekhtman[10,11]

Preprint, 2010 March 21

Abstract.   The Gamma-Ray Burst Monitor (GBM) on the Fermi Gamma-ray Space Telescope detected 12 intense Terrestrial Gamma-ray Flashes (TGFs) during its first year of observation. Typical maximum energies for most of the TGFs are $\approx$ 30 MeV, with one TGF having a 38 MeV photon; two of the TGFs are softer and longer than the others. After correcting for instrumental effects, a representative bright TGF is found to have a fluence of $\sim$0.7 photons cm^{-2}. Pulses are either symmetrical or have faster rise times than fall times; they are well fit with Gaussian or log-normal functions. The fastest rise time observed was 7 μs, constraining the source radius to be less than about 2 km from the velocity of light. TGFs with multiple pulses separated in time have been known since their discovery; the GBM sample also includes clear cases of partially overlapping pulses. Four TGFs are associated with lightning locations from the World Wide Lightning Location Network (WWLLN). With the several μs absolute time accuracy of GBM, the time order can be confidently identified: one TGF occurred before the lightning, two were simultaneous, and one TGF occurred after the lightning.

1. Introduction

Terrestrial Gamma-ray Flashes (TGFs) were discovered with the BATSE instrument on the Compton Gamma-Ray Observatory [*Fishman et al.*, 1994], and have since been observed with RHESSI [*Smith et al.*, 2005; *Grefenstette et al.*, 2009], AGILE [*Fuschino et al.*, 2009; *Marisaldi et al.*, 2009] and now with the Gamma-ray Burst Monitor on the Fermi Gamma-ray Space Telescope. TGFs consist of one or occasionally multiple pulses of gamma-rays, each pulse typically lasting less than a millisecond. The gamma-ray spectra extend to at least 25 MeV. A small fraction of TGFs are observed mostly or entirely as electrons [*Dwyer et al.*, 2008]. The BATSE observations indicated a correlation with thunderstorms, an association which was strongly confirmed with RHESSI. The spectrum is well explained by bremsstrahlung emission from electrons accelerated to high energies by the Relativistic Runaway Electron Avalanche (RREA) process [*Gurevich et al.*, 1992; *Dwyer*, 2003]. The origin of the strong electric fields required for the RREA process is less certain. For example, the avalanche region could be located in the high fields produced in thunderclouds before lightning, in the high fields produced during lightning, or in the fields above the cloud after a lightning discharge [*Fishman et al.*, 1994; *Roussel-Dupré and Gurevich*, 1996; *Lehtinen et al.*,

1999; *Inan and Lehtinen*, 2005; *Dwyer and Smith*, 2005; *Milikh et al.*, 2005; *Williams et al.*, 2006; *Carlson et al.*, 2007; *Babich et al.*, 2007; *Dwyer*, 2008].

2. Gamma-ray Burst Monitor

The Fermi Gamma-ray Space Telescope consists of two instruments designed to observe gamma-rays: the Large Area Telescope (LAT) and the Gamma-ray Burst Monitor (GBM). The LAT is a pair-conversion telescope designed to cover the energy range of 20 MeV to more than 300 GeV [*Atwood et al.*, 2009]. GBM has twelve Sodium Iodide (NaI) scintillator detectors to cover the energy range $\approx$8 keV to 1 MeV and two Bismuth Germanate (BGO) scintillators to cover the energy range $\approx$200 keV to $\approx$40 MeV. The detectors are arranged on the spacecraft to view the entire unocculted sky with nearly uniform sensitivity. GBM was primarily designed to observe Gamma-Ray Bursts (GRBs), but provides useful observations for many other sources. Here we report the first observations of TGFs with GBM.

Fermi has a nearly circular orbit of 565 km altitude with an inclination of 25.6°; this causes it to spend long times over areas in the tropics where thunderstorms are common. In the normal viewing mode of Fermi, the LAT viewing axis is pointed 35° off the zenith and the Earth is underneath the viewing direction. However, TGFs have such energetic spectra that their photons can be detected through the rear of GBM detectors, or even through the spacecraft.

Like BATSE, but unlike RHESSI, GBM TGF data are obtained by a "triggering" process. Normally only data with relatively coarse time bins are telemetered to the ground. When the GBM flight software detects a statistically significant rate increase it "triggers" and turns on a data mode, Time-Tagged Events (TTE), in which the arrival times and energies of individual photons are transmitted to the ground. The GBM instrument is further described in Appendix A and by *Meegan et al.* [2009] and *Fishman et al.* [2010]; the data set used herein is described by *Fishman et al.* [2010].

3. The TGFs

GBM triggered on 12 TGFs during the first year in which triggering was enabled, starting on 11 July 2008. The properties of these TGFs are summarized in Table 1. The events of this sample have common properties with each other and with TGFs seen by previous instruments that enable us to identify them as TGFs. The events are detected in multiple GBM detectors, discriminating against statistical fluctuations. They are much shorter and have higher mean photon energies than GRBs. Two triggers with distinct characteristics appear similar to TGFs but are instead caused by showers from > 100 TeV cosmic rays, as shown by simultaneous

[1]CSPAR, University of Alabama in Huntsville, Huntsville, AL, 35899, USA

[2]Space Science Office, NASA Marshall Space Flight Center, Huntsville, AL, 35812, USA

[3]Dept. of Physics, University of Alabama in Huntsville, Huntsville, AL, 35899, USA

[4]ISR-1, Los Alamos National Laboratory, Los Alamos, NM 87545, USA

[5]Max-Planck Institut für extraterrestrische Physik, D-85741 Garching, Germany

[6]Universities Space Research Association, Huntsville, AL, 35803, USA

[7]Physics and Space Sciences, Florida Institute of Technology, Melbourne, FL 32901, USA

[8]Dept. of Physics, University of California, Santa Cruz, Santa Cruz, CA 95064, USA

[9]Earth and Space Sciences, University of Washington, Seattle, WA 98195, USA

[10]Space Science Division, U. S. Naval Research Laboratory, Washington, D.C., 20375, USA

[11]George Mason University, Fairfax, VA, 22030, USA

signals in the LAT calorimeter (Appendix B). Fig. 1 shows the locations of Fermi when the TGFs were detected. If TGFs originate below ~50 km altitude, their locations are likely to be within several hundred kilometers of the sub-spacecraft points because larger offsets would require longer path lengths through the atmosphere and high attenuation of gamma-rays. The locations are consistent with regions of high thunderstorm activity, as expected (cf. Fig. 1 to the RHESSI TGF map [*Smith et al.*, 2005] or to a lightning map [*Christian et al.*, 2003]).

We use the duration measure t_{90}, which is commonly used for GRBs, to measure the durations of the TGFs (Table 1, Fig. 2). The t_{90} value is the length of the central interval in which 90% of the counts are accumulated, with 5% of the counts occurring before and after the interval. Two TGFs, 081113 and 090627 have distinct emission episodes separated by gaps without detectable emission. For these TGFs, we apply the t_{90} technique to each episode rather than to the entire TGF so as not to include the emission gaps in t_{90}. (This differs from the normal usage for GRBs.) The rise and fall times listed in Table 1 are obtained from fitting the profiles of the TGFs (next section).

The 12 GBM TGFs have similar total numbers of counts – this is most likely an instrumental selection effect, in which GBM is triggering on only the brightest TGFs, which are also only just above the trigger threshold. (In contrast to the in-orbit analysis using 16 ms resolution data, the GBM TGFs are highly significant by ground analysis at higher temporal resolution.)

Fig. 3 shows the time profiles of the twelve TGFs, while Figure 4 shows scatter plots of individual detected counts in the BGO detectors from selected TGFs. From Figs. 3 and 4 it is apparent that TGFs vary in their temporal and spectral characteristics.

Fig. 4 and similar data for the other GBM TGFs [*Fishman et al.*, 2010] show spectral differences among the events. The raw spectra should be interpreted with caution: simulations show that spectral distortions from pulse pileup (Appendix A) are significant for input rates $>\approx$ 300 kcps. TGF spectra have more low energy photons than high energy photons, so the simulations predict that low energy photons may align to produce counts with apparently higher energies, resulting in measured count spectra that are reduced in amplitude at low energies, and increased at medium energies. High energy photons are so rare that two are unlikely to arrive simultaneously and so major shifts of their energies are unlikely. The more common effect for high energy photons, which occurs at all rates, is that some of the energy will escape the crystal and the measured energy of the count will be an underestimate of the photon energy. Based on this analysis, some preliminary statements are possible. Most of the TGFs have photons with energies up to $\approx$30 MeV, for example, Fig. 4 for 081001 shows numerous counts to 30 MeV and one at $\approx$38 MeV. (AGILE has reported one TGF with a 43 MeV detection [*Marisaldi et al.*, 2009].) The exceptions in the first twelve GBM TGFs are TGFs 080807, 081113, 090510 and 090627. The two TGFs with separated pulses (Fig. 5) have lower spectral cutoffs: TGF 090627 has a hard spectrum with numerous counts to 20 MeV, while the spectrum of TGF 081113 ends at about 13 MeV. TGFs 080807 (Fig. 4) and 090510 appear distinct from the other TGFs: not only do their spectra end at 10 or 12 MeV (ignoring isolated overflow counts that are likely background), but they are much longer than the other TGFs, with t_{90} durations of 3.08 and 2.08 ms, respectively.

4. Pulses

The TGF time profiles are analyzed by fitting with simple functional forms, plus a constant background rate. The fits are made to the TTE data of all 14 GBM detectors at

the intrinsic 2 μs resolution of the data and thus do not depend on the histogram binning (Fig. 3). Some pulses appear symmetrical, while others are clearly asymmetrical, with tails. For the TGF pulses that are symmetrical, the Gaussian function is used to fit the time profiles,

$$f(t) = \frac{A}{\sqrt{2\pi}\sigma} \exp\left[-\frac{1}{2}\left(\frac{t-t_p}{\sigma}\right)^2\right], \quad (1)$$

with three free parameters, amplitude A (counts per s), peak time t_p (s) and width σ (s). For asymmetric pulses, the log-normal function [*Aitchison and Brown*, 1969] is used,

$$f(t) = \frac{A}{\sqrt{2\pi}\sigma(t-t_s)} \exp\left[-\frac{1}{2}\left(\frac{\log\frac{t-t_s}{\tau}}{\sigma}\right)^2\right] \quad (2)$$

for $t > t_s$, otherwise $f(t)$ is zero. The four free parameters of the function are amplitude A (counts per s), start time t_s (s), shape σ and time scale τ (s). (Some common representations for the log-normal use $\mu \equiv \log\tau$ or set $t_s \equiv 0$; the former is an alternative parameterization, while the latter is a simpler form which is inappropriate for TGFs since they occur at arbitrary times.) For the log-normal, the peak time can be calculated as [*Aitchison and Brown*, 1969]

$$t_p = t_s + \exp(\log\tau - \sigma^2). \quad (3)$$

In both cases the fits also include a constant background rate B counts per second, not due to the TGF, so that the model counts in a 2 μs TTE time bin i are

$$M_i = 2\,\mu s\,(f(t_i) + B). \quad (4)$$

The functions are fit to the TTE data to maximize Poisson likelihood

$$\log\mathcal{L} = \sum_i\left(O_i\log M_i - M_i - \log O_i!\right), \quad (5)$$

where O_i are the observed counts in TTE time bin i.

The profile fits work well considering the simple functions used (Gaussian or log-normal) – only a few histogram bins (Fig. 3) deviate by as much as two sigma from the curves. If Gaussians are used for all of the pulses, worse results are obtained for pulses that appear asymmetrical (Fig. 6).

The rise and fall times listed in Table 1 are the times between the 10% and 90% levels of the fitted curves. These fits are made to the raw TTE data without deadtime corrections. Since these fits underestimate the peaks, the true rise and fall times are actually more rapid. Obviously the fits made with Gaussians produce equal rise and fall times. All of the log-normal fits produced shorter rise times than fall times.

TGF 081113 and TGF 090627 have separated emission episodes (Fig. 5), with gaps lacking emission lasting 1.1 and 7.75 ms, respectively. We use the term "emission episode" rather than pulse because one of these episodes consists of two pulses (the second episode of TGF 090627). Three of the four emission episodes in these two TGFs are the weakest in the sample. GBM would probably not have triggered on either episode of TGF 081113 had they not fallen within the same 16 ms trigger window. Indeed, for TGF 090627 the two episodes were not in the same 16 ms window and GBM triggered only on the second episode, which is much stronger. This lends support to the our conclusion that the similarity of count fluence among the sample is a selection effect.

TGF 090522 (Fig. 3) and emission episode 090627b (Fig. 3) both consist of two pulses that partially overlap. Without the recognition of the overlapping pulses, these events would seem anomalous – they would be interpreted as single pulses with slower rise times than fall times.

5. Intensity

GBM has non-paralyzable deadtime (Appendix A) so that the observed count rate m can normally be corrected into the true rate f using $f = m/(1 - m\tau_{GBM})$, where τ_{GBM} is the deadtime per event (i.e., 2.6 μs) [*Knoll*, 2000]. However, this equation assumes that both m and f are long term averages, whereas the intensity of TGFs varies on timescales $\sim 10\tau_{GBM}$ and so a simple deadtime inversion in not possible. Instead the incident intensity history is deduced using a deconvolution method: a parameterized functional shape for the pulse profile is assumed and simulations are performed to determine the expected observed counts in GBM. The parameter values of the assumed pulse profile are fit to match the simulated counts to the data. A disadvantage of this method is there is no theoretical prediction for the shape of a TGF and no unique choice for the functional shape to use in the deconvolution.

TGF 081001 was selected for analysis as representative of high intensity GBM TGFs (long TGFs such as 080807 or 090510 have lower deadtime.) Advantages of TGF 081001 includes its known location (Table 2) and, for the BGO detectors, a lack of counts in the highest channel, which has a longer deadtime. The simulations are in the time domain and have no spectral dependence. Assuming a low background rate and a particular function with particular parameter values for the pulse profile, a sequence of Poisson-distributed photons is created using the thinning method for a nonhomogeneous (variable-rate) Poisson process [*Lewis and Shedler*, 1978; *Rebinstein and Kroese*, 2008]. The photons are then dead-time filtered, removing photons that follow within 2.6 μs of an accepted photon. The simulated deadtime-filtered photons are binned at 2 μs resolution to match the resolution of GBM Time-Tagged Event (TTE) data, to create a single simulated observation of a TGF with GBM TTE data. Many simulations create the mean expected counts M_i for each 2 μs TTE bin i. The parameter values are adjusted, according to Poisson likelihood (eq. 5), to obtain the best fit between the simulated expected model counts and the observed counts. The likelihood fitting is done at the full resolution of the TTE data.

Figure 7(left) shows the result of fitting the data of the two BGO detectors for TGF 081001, assuming a Log-Normal profile – the difference between the simulated observations with and without deadtime indicate that only 51% of the photons incident on the BGO detectors were processed; during the peak 40 μs bin this fell to 40%. The fit indicates that the deadtime-corrected fluence of this TGF is 110±10 counts per BGO detector, with a peak flux of 23 ± 4 counts in 40 μs. The effective area of a BGO detector is ≈ 160 cm^{-2} over most of the energy range, indicating a fluence of $\sim$0.7 photons cm^{-2} and a 40 μs peak flux of $\sim$3600 photons cm^{-2} s^{-1}.

The fits to the sum of all 14 detectors (Fig. 3) indicate that Log-Normal is a better representation for this GRB than a Gaussian. Nevertheless, it is useful to use a Gaussian to determine the dependence of the results on the profile function used. With just the BGO data, the Gaussian deconvolution is slightly worse than the Log-Normal fit, but still fully acceptable – Fig. 7(right) The values are quite similar: a fluence of 105 ± 20 counts per BGO detector and a peak 40 μs flux of 26 ± 5 counts. The corresponding live-times are 49% and 37%.

6. Correlations with lightning

TGFs have long been associated with thunderstorms and lightning. Lightning strokes produce very-low frequency (VLF) radio signals, sferics, which can be used to detect and locate the strokes at large distances. Using radio detection, efforts have been made to determine the relative timing of TGFs and lightning, but the relation has not been conclusively established. Four BATSE TGFs have associated sferics, with the TGFs following the sferics by $\sim$ 1 to 3 ms [*Inan et al.*, 1996; *Cohen et al.*, 2006]. The accuracy of this timing comparison was limited by the time standard of the radio to $\sim$ 1 ms. A larger number of associations have been found for RHESSI TGFs, with the results having a dispersion of several ms, typically with a mean offset of TGFs preceding sferics. [*Cummer et al.*, 2005; *Stanley et al.*, 2006; *Inan et al.*, 2006; *Lay*, 2008; *Cohen et al.*, 2010]. The small number of associations for BATSE TGFs, in combination with the 1 or 2 ms uncertainty in the absolute accuracy of the RHESSI clock [*Grefenstette et al.*, 2009] has precluded a firm conclusion on the order of TGFs and sferics. GBM has absolute time accuracy of several μs (Appendix A).

The World Wide Lightning Location Network (WWLLN) is an effort to locate lightning anywhere on the globe with high temporal and positional accuracy. WWLLN can locate individual strokes to within 10 km of their origin with a mean timing error of 30 μs by using the arrival times of the sferic wave packets detected at five or more VLF receiving stations. The WWLLN detection efficiency was estimated as about 3% in 2007, though this efficiency varies according to position on the Earth, time of day and stroke peak current [*Rodger et al.*, 2009]; since then the detection efficiency has increased as the number of stations has increased. WWLLN is most efficient at detecting cloud-to-ground (CG) lightning but is also sensitive to some intra-cloud (IC) lightning. IC lightning has been associated with TGFs [*Stanley et al.*, 2006; *Williams et al.*, 2006].

We searched for associations between GBM TGFs and WWLLN lightning locations within 500 km of the sub-satellite position and for lightning times, corrected for light travel time to the lightning position, within 5 ms of the TGF peak. Applying these criteria to the first twelve GBM TGFs, four closely-related WWLLN locations are found (Table 2). To estimate the probability of these matches occurring by chance, controls were created for each of these four TGFs by offsetting from the actual peak time of the TGF in 1 second increments from 500 seconds before to 500 seconds afterwards, creating 1000 controls per TGF. (The average rate of WWLLN lightning detections within 500 km remained constant over the $\pm$500 s span of the controls so that $\pm$500 s is a suitable interval to measure the rate of false matches. Owing to the variation in lightning stroke density from storm to storm, and the varying efficiency of the WWLLN network with geographical location, time of day, and improvement with time, the controls for the various TGFs are not homogeneous.) A search for temporal and geographical matches of the controls with locations in the WWLLN database found no control matches for three of the four TGFs, and two amongst the controls for TGF 081123. We therefore infer the probability of a spurious TGF-WWLLN location match is < 0.001 for TGFs 081001, 081113 and 090203 and is $\approx$ 0.002 for TGF 081123 – we therefore conclude that the 4 TGF-WWLLN pairs are most likely true associations (Table 2)

One of the TGFs has two separated pulses in the GBM data, and the offset times relative to the closest WWLLN location (the same one in each case) are listed separately in Table 2. In column 4, the temporal offset from the peak of the TGF emission is shown, corrected in column 9 for two effects. First, the offset is corrected for the light travel time between a source, assumed to be 20 km above the Earth, and the altitude of Fermi (column 3). Additionally, the GBM time is corrected for the drift of the GBM clock between GPS synchronizations (Appendix A) – the maximum clock correction was 14 μs for TGF 081001. The uncertainty in the time offset varies according to the accuracy of

the WWLLN data for each stroke (column 10), which reflects both the number of stations that made the measurement and the accuracy of the equipment at these stations. There are TGF-WWLLN pairs with timing offsets significantly different from zero, compared to the timing errors (GBM, WWLLN, and the choice of fiducial times on the TGF and sferic), with both signs – TGF 090203 with a negative offset occurred before the lightning stroke, while TGF 081001 with a positive offset occurred after the lightning stroke.

We also made an extended search to 1000 km radius from the sub-satellite position, with the same ±5 ms window corrected for light travel time, and found no additional associations.

For the eight GBM TGFs which are not associated with a particular WWLLN-detected lightning stroke, we searched the WWLLN data for storm systems that might be the source of the TGF by testing for a concentration of WWLLN-detected strokes within 500 s of the TGF and 500 km of the sub-spacecraft position. This technique identifies storm systems for six of the eight, with only TGFs 080807 and 090510 remaining uncorrelated with WWLLN lightning locations. For TGF 080807, several strong storms are located at the northern end of the magnetic field line through Fermi, making it possible that this TGF was produced by electrons that traveled along the magnetic field lines from one of these storms [Dwyer et al., 2008; Carlson et al., 2009]. Neither of the magnetic footprints for the spacecraft position of TGF 090510 are associated with concentrations of lightning that would indicate a storm. The lack of an identification for 090510 may be due to its location over Africa, where the WWLLN station density is lower.

7. Interpretations

Probably all TGF samples are modified by selection effects, either from detector characteristics, triggering (BATSE, AGILE & GBM) or the ground detection algorithm (RHESSI). GBM has a low TGF detection rate compared to RHESSI, and the GBM TGFs have relatively little variations in their total number of counts. This shows that GBM, with its onboard trigger algorithms (Appendix A), is only able to trigger on the brightest TGFs. With one exception, GBM TGFs are contained in a 16 ms trigger integration, so GBM is triggering based upon total counts of a TGF rather than peak flux. The measured count total is reduced for the shortest TGFs because of deadtime. The BATSE TGF sample is weighted toward long and multi-pulse events [Nemiroff et al., 1997], which was caused by the BATSE detector rates saturating for short, intense events due to deadtime, preventing the accumulation of sufficient counts to trigger [Grefenstette et al., 2008]. GBM is less affected by deadtime than BATSE and the GBM sample has a lower fraction of long and multi-pulse TGFs. The GBM selection effect for very bright events could overweight electron events because of their expected higher intensities (charged particles follow a magnetic field line, while photons disperse) [Dwyer et al., 2008; Carlson et al., 2009] and longer durations.

TGF 080807 (Figs. 3 & 4) is the longest TGF in the first year, with $t_{90} = 3.08$ ms. It is also the only TGF detected during the first year to have an asymmetric detection pattern, with many counts in the detectors on one side of the spacecraft and extremely few or no counts in the detectors on the other side (Fig. 4A shows source counts in BGO 0, but no clear signal above background in BGO 1; also see Fishman et al. [2010]). The other eleven TGFs reported in this paper have more symmetrical detections, with signals in all detectors, and typically nearly equal rates in the detectors

of the same detector type (NaI or BGO). (e.g., see Fishman et al. [2010] for 081025). TGF 090510 (Fig. 3) has the second longest duration ($t_{90} = 2.08$ ms). Both of these TGFs have atypically soft spectra (Fig. 4A for 080807). The long tails of these two TGFs are much too long to be explained as photons delayed via Compton scattering; these TGFs may be electron beam events – dispersion in the arrival times of electrons with different pitch angles could produce the longer durations [Dwyer et al., 2008].

Some of the GBM TGF pulses are consistent with symmetry and were fit with Gaussians (e.g., Fig. 3: pulse TGF 081113a: and TGF 081223), while others are clearly asymmetric. BATSE light curves were found to be consistent with symmetry (asymmetry was found in lower-energy photons lagging higher-energy photons) [Nemiroff et al., 1997]. The asymmetric GBM TGF pulses are well fit with log-normal functions and have fall times that are longer than their rise times. The second pulse of TGF 081113, (Fig. 3 – 081113b) has a 7 μs rise and 100 μs fall, while TGF 081123 (Fig. 3) has a 30 μs rise and 130 μs fall. Others have longer tails, up to 160 μs (Table 1). The possible electron events, 080807 and 090510, are very asymmetrical and have even longer tails. These tails are probably too long to explain as photons delayed by Compton scattering: RHESSI observations and simulations indicate delays of lower-energy photons of about 30 μs [Grefenstette et al., 2008].

TGF 090522 and emission episode 090627b (Fig. 3) appear to have slower fall times then rise times – this is because these emission episodes consist of two overlapping pulses with the first pulse having longer timescales than the second. TGF 090627 has episodes separated by a 7.75 ms gap, so that TGF 090627 consists of three pulses in two groups (Figs. 3). TGFs with separated pulses, such as GBM TGFs 081113 and 090627, have been previously observed [Fishman et al., 1994]; the observation of close, partially overlapping pulses shows that TGF process is capable of multiple, apparently independent initiations on timescales as short as one-quarter of a ms – theories will need to explain how distinct pulses are created so closely in time.

Three pulses in the first year have t_{90} values of 0.16 or 0.18 ms – the pair of TGF 081113 and TGF 081123. These pulse durations set upper limits, from light travel time, on the emission region radii of 54 km. More stringent limits can be set from variablity timescales – the second pulse of TGF 081113 (Fig. 3 – 081113b) has the fastest rise time, 7μs, which corresponds to a radius of 2.1 km. If lightning propagation velocities are used instead of the speed of light, much smaller sizes are obtained [Dwyer, 2008].

TGF 081001 is a typical bright GBM TGF with a fluence of ~ 0.7 photons cm^{-2}. To find the corresponding TGF energy, we used the avalanche code of Dwyer [Dwyer and Smith, 2005; Dwyer, 2007] to compare the total energy of relativistic electrons in the avalanche with their bremsstrahlung production, and GEANT3 to propagate the photon spectrum (approximated as $\exp[-E/7.3$ MeV$]/E$) through a model of Earth's atmosphere. Our initial photon beam had an opening half-angle of $30°$ and a source altitude of 21 km in a model of the US Standard Atmosphere. Averaging over a 300 km radius at low-Earth orbit (580 km) we found 1.16×10^{-16} photons cm^{-2} per initial photon. The average photon energy above 30 keV of the input spectrum is 1.43 MeV, giving 1.4 kJ of input photon energy to match the TGF fluence at orbit. This is higher than the estimate of Carlson et al. [2007] for the maximum photon energy of TGFs observed with RHESSI and BATSE (about 1 kJ for the very brightest events, for 21 km and $45°$), but perhaps consistent considering detailed differences between the simulations. Our estimate is expected to be higher considering the recent understanding of deadtime in those two instruments [Grefenstette et al., 2008, 2009], and the deadtime correction included in the fluence value ~ 0.7 photons cm^{-2}.

The avalanche code, which tracks bremsstrahlung production both during the continuous acceleration of the electrons in the field region and their subsequent stopping afterwards, allows us to also calculate the maximum instantaneous energy in relativistic electrons (7.0 kJ) and the total energy deposited in the atmosphere by the energetic electrons and gamma-rays (22 kJ).

In addition to deadtime, simulations show that the spectra of the most intense GBM TGFs are modified by pulse pileup. Since the BATSE Large Area Detectors had large collecting areas, pulse pileup is also a likely effect for intense TGFs in the BATSE sample – some previous analyses should be revisited.

Because the WWLLN detects only a fraction of all lightning strokes, the absence of associations for some TGFs is not surprising. The association rate of 4 out of 12 for GBM and WWLLN is inconsistent with the 4.3% rate found between RHESSI and WWLLN [*Lay*, 2008] at the 0.2% level [*Smith et al.*, 1996]. One explanation is that the GBM sample typically consists of more intense TGFs than the RHESSI sample, and that more intense TGFs might be correlated with the higher current lightning strokes, which have a higher WWLLN detection efficiency. *Rodger et al.* [2009] found the the WWLLN detection efficiency for high-current lightning strokes in 2007 to be ≈30%, which matches the association rate between GBM TGFs and WWLLN lightning strokes, however, this may be a coincidence since the GBM sample is small. Another possibility is that the WWLLN detection efficiency has increased over time, owing both to a growth in the number of WWLLN receiving stations and to improvements in the WWLLN location algorithm.

For each TGF, column 7 of Table 2 lists the angle between the zenith direction at the source and the direction from the source to Fermi. If these TGFs are vertically oriented, their beaming half-angles, including the beam-width increase caused by Compton scattering, must be at least as large as these angles. The largest values are ≈ 30°. Competing effects are that there is more area at larger offsets from Fermi, but also greater path lengths through the atmosphere and hence greater attenuation. Additionally, GBM is triggering on more intense TGFs and is less likely to detect TGFs at higher angles. Previous papers have typically specified offsets in units of distance from the sub-satellite point (column 8 of Table 2). Based on the large width of the distribution and the similar altitudes of Fermi (542 to 570 km) and RHESSI (543 to 601 km: http://scipp.ucsc.edu/~dsmith/tgflib_public/tgflist.txt), the offsets found with the two instruments can be meaningfully compared in units of distance. Accurate offset measurements of RHESSI TGFs based on geolocation of sferics using three or more VLF receivers have found most offsets to be 300 to 400 km or less, but with some offsets extending to ∼ 700 km [*Stanley et al.*, 2006; *Lay*, 2008; *Hazelton et al.*, 2009; *Cohen et al.*, 2010]. The offsets found for GBM TGFs, ranging up to 290 km, agree with the values most commonly found for RHESSI TGFs. Since this sample is small this is not a strong test for existence of a tail past 400 km to the offset distribution.

Efforts to correlate TGFs to lightning strokes measured with sferics have so far not reached a firm conclusion on the temporal order of TGFs and sferics. Issues include the dispersion in the measurements, the small number of sferics associated with BATSE TGFs and the uncertainty in the absolute time base of RHESSI [*Grefenstette et al.*, 2009]. Additionally, the measurements for BATSE found the TGFs to follow the sferics [*Inan et al.*, 1996; *Cohen et al.*, 2006], while some observations show RHESSI TGFs preceding their associated sferics [*Cummer et al.*, 2005; *Stanley et al.*, 2006; *Inan et al.*, 2006; *Lay*, 2008; *Cohen et al.*, 2010]. GBM time is derived from GPS and has high absolute accuracy (Appendix A) so that time differences between GBM and WWLLN have errors much smaller than some TGF-WWLLN offsets. The observations (Table 2) show that either the TGF or the lightning stroke can be first. There are at least three possible explanations. A chance match for either of the non-simultaneous cases, TGFs 081001 and 090203, cannot be totally ruled out but is unlikely because of the lack of spurious matches in the 1000 controls for each TGF. Another possible explanation is that the lightning type that is associated with TGFs has multiple strokes that are separated by several milliseconds. When WWLLN detects the stroke directly associated with the TGF, the time offset is zero, but when it detects a different stroke in the lightning sequence, the offset can be several milliseconds, either negative or positive, depending on whether the detected stroke was before or after the stroke that is directly associated with the TGF. Multiple sferics were observed for some RHESSI TGFs [*Cohen et al.*, 2010]. The several millisecond offsets are comparable to the spacing of emission episodes of some TGFs: BATSE TGF 1457 had five pulses over 10 ms [*Fishman et al.*, 1994; *Nemiroff et al.*, 1997], and the GBM sample includes TGFs with emission gaps of 1.1 and 7.75 ms. Alternatively, the combination of a clear association between some TGFs and radio-detected lightning strokes, but the lack of a consistent order, could indicate that a third factor triggers both the TGF and the lightning stroke.

7.1. Summary

GBM detected twelve TGFs in its first year of operation. These TGFs had very similar total number of counts, most likely due to the GBM only triggering on the most intense TGFs. Typically these TGFs have photons with energies up to ≈ 30 MeV, and in one case as high as 38 MeV, but two of the TGFs are distinctive, being both much longer and softer than the others. These two TGFs, 080807 and 090510, may be electron events.

TGFs with separated pulses are well known – GBM now clearly detects partially overlapping pulses. For example, TGF 090627 shows both behaviors: it has one isolated pulse, and then 7.75 ms later, two partially overlapping pulses with peak times that differ by only 0.26 ms. The observation of partially overlapping pulses implies that TGFs must be able to start pulses, apparently independently, on short timescales. The fastest rise time observed was 7 μs, which sets an upper-limit on the source radius of about 2 km. Both symmetric and asymmetric pulses were observed. The asymmetric pulses always have longer fall times than rise times. The symmetric pulses are well fit with the Gaussian function, the asymmetric pulses with the Log-Normal function.

GBM, like other TGF instruments so far, has substantial deadtime at the peaks of bright TGFs. A simple deadtime analysis is inadequate because the rates of TGFs vary on timescales comparable to the GBM deadtime per photon. Instead, a deconvolution method was used. A typical bright GBM TGF, TGF 081001, is found to have a fluence of ∼0.7 photons cm^{-2} and a 40 μs peak flux of ∼3600 photons cm^{-2} s^{-1}.

We searched for associations between GBM TGFs and lightning locations observed with WWLLN (i.e., VLF sferics). Four close associations were found, exhibiting all three possible temporal orders: the TGF before the sferic, simultaneous, and after. The association rate of four out of twelve TGFs is unexpectedly high compared to the rate obtained with RHESSI and WWLLN – this could be due to the effect of GBM selecting bright TGFs, or due to improvements to WWLLN with time. The offsets of the WWLLN locations from the sub-satellite positions are less than 300 km and are consistent with previous findings.

A new version of the GBM flight software, with revised trigger algorithms using data from the BGO detectors, was uploaded on 10 November 2009. The revised algorithms have increased the GBM TGF trigger rate, and are also detecting weaker TGFs.

Appendix A: GBM

GBM has twelve Sodium Iodide (NaI) scintillation detectors to cover the energy range ≈8 keV to 1 MeV. Each has dimensions 12.7 cm diameter and thickness 1.27 cm. The NaI detectors are oriented to point in various directions to observe the entire sky that is unocculted by the Earth. The different orientations are used in combination with the approximately cosine angular responses at lower energies to locate GRBs and other sources. However, the NaI detectors have a more uniform angular response to the exceptionally high-energy gamma-rays of TGFs, which makes this location method difficult to implement.

GBM also has two Bismuth Germanate (BGO) scintillation detectors on opposite sides of the spacecraft to cover the energy range ≈200 keV to ≈40 MeV. These detectors are cylinders of diameters 12.7 cm and lengths of 12.7 cm. The high density of BGO and the high atomic number of Bi give BGO an excellent response to high-energy gammarays: the full-energy absorption response of a BGO detector is ≈ 100 cm^2 to 2 MeV, remains above 50 cm^2 to 17 MeV and above 20 cm^2 to 40 MeV. The effective area of a BGO detector is ≈160 cm^2 for all energies > 300 keV. In comparison, the full-energy-absorption response of the thin NaI detectors falls steeply above 200 keV. The energy range and response of the BGO detectors make them very well suited for observing TGFs.

All fourteen GBM detectors operate continuously, except when Fermi is in the South Atlantic Anomaly (SAA), a region of high fluxes of trapped charged particle (Fig. 1). To reduce the data volume, GBM telemeters to the ground coarsely time-binned continuous data and increases the data volume when an interesting event is detected by the flight software (FSW) on-board GBM. The FSW monitors the rates of the detectors and autonomously triggers when a statistically significant rate increase is detected in two or more NaI detectors. Detector rates are monitored on timescales ranging from 16 ms to 8.192 s and over four energy ranges: 25 to 50 keV, 50 to 300 keV, >100 keV and >300 keV. A drawback of this approach for TGFs is a hardware limitation that the minimum sampling interval for triggering is 16 ms, which is much longer than most TGFs, thereby diluting the signal of TGFs with background and reducing the sensitivity of GBM to triggering on TGFs. Additionally, the original FSW triggering algorithms, which were designed for GRBs, only used the data of the NaI detectors. Improved FSW triggering algorithms that increase the sensitivity to TGFs by using BGO detector data were implemented on 10 November 2009, after the period of this dataset.

With the original trigger algorithms, all of the TGFs have been detected on the 16 ms timescale, and with one exception the energy ranges were either above 300 keV (most common) or above 100 keV. The trigger threshold for these two algorithms is an 8.0σ increase above the background rate. The significances of the first 12 GBM TGFs, as calculated on board GBM using 16 ms resolution data, ranged from 8.3σ to 10.5σ.

The trigger time (Table 1) is the end time of the data interval which contained the rate increase which caused the FSW to trigger. For TGFs, the data interval will be 16 ms long and typically the TGF will be entirely before the trigger time.

When GBM triggers, additional data are telemetered to the ground, including Time-Tagged Events (TTE), which is most useful data type for TGFs. This data type records individual counts received by the detectors, either photons or background particles, reporting the arrival times and measured energy losses (which may be either a portion or the entire energy of an incident photon) with 2 μs time resolution and 128 channel spectral resolution using pseudologarithmic channels spaced over the energy range of the detector. The GBM raw data has an absolute time accuracy of at least 20 μs based on synchronization at 1 Hz to

GPS time of 2 μs absolute accuracy. In between the 1 Hz synchronizations the GBM time base is a quartz oscillator, with a frequency that varies from nominal according to temperature – the resulting drift before the next synchronization can be as large as 20 μs. The drift is corrected using the measured temperature of the oscillator, achieving an absolute time accuracy of several μs. The time coverage of TTE is from ≈ −30 s before the trigger time, using a ring buffer that is latched at trigger time, to 300 s after the trigger time.

The signals from the PMTs of the detectors are converted to bipolar pulses with an ≈0.22 μs risetime and a several μs recovery to baseline. To reduce spectral distortions from overlapping pulses, the system is intentionally dead for 2.6 μs after the peak of a regular pulse that was processed by the electronics and 10.4 μs after a pulse which is off-scale. Off-scale pulses are placed into the highest channel, which is termed the "overflow channel". Pulses that are not processed by the electronics do not cause deadtime. This results in a non-paralyzable deadtime with a very weak spectral dependence due to the overflow channel.

If two or more pulses arrive so closely that they overlap, the heights of the pulses on the waveform will be modified. Very closely spaced pulses can merge and appear to be a single pulse of higher energy. If a peaks falls on the long tail of opposite sign of another pulse, its amplitude will be reduced – the deadtime is designed to prevent analysis of such peaks, but this only works if the first pulse was analyzed by the pulse height electronics. These phenomena are referred to as "pulse pileup".

Appendix B: Cosmic Ray Triggers

GBM triggers 090403.218 and 090408.585 were initially classified as TGFs based on their short durations, highenergy spectra, and pattern of being detected in all GBM detectors. These events have several distinctive features: a) they began simultaneously in all 14 GBM detectors. All 14 detectors recorded a count in the same 2 μs TTE time bin, for a simultaneous start at the finest time resolution available in the GBM data. b) The initial counts were in the overflow channels (or one channel less, for BGO 0 and trigger 090408.585), indicating that the initial counts were either of very high energies, or were of such high rates that many counts merged in less than 2 μs to deposit a large amount of energy. Examples of these features can be seen in Fig. 8, which show the first BGO counts from these events simultaneous in time and occurring in the overflow channel. Additionally, c) the BGO spectra show a peculiar spectral gap between the very high energies of the initial counts and all the following counts, all of which are below 10 MeV. These events were relatively long, with t_{90} durations of 1.3 and 1.0 ms, respectively.

The initial GBM counts of these two events are simultaneous with large energy deposits in the LAT Calorimeter. GBM trigger 090403.218 corresponds to a measurement of 37 TeV in the LAT Calorimeter, and 090408.585 to 45 TeV. These are amongst the highest energy deposits ever observed in the LAT Calorimeter. In both cases all CsI crystals of the LAT Calorimeter recorded signals, ranging from >50 MeV to >65 GeV, the energy at which the crystal readout saturates. Our interpretation is that a high-energy (> 100 TeV) cosmic ray proton or nucleus interacted in the Calorimeter, creating a shower of secondaries. The numerous secondaries reached all crystals of the Calorimeter, and also all 14 GBM detectors.

The cosmic-ray shower explains the simultaneous initial counts in all 14 GBM detectors. The long durations of the GBM events also needs to be explained. While NaI has long-lived phosphorescence components, such components are much reduced in BGO [Knoll, 2000]. A likely explanation is that the numerous ∼GeV secondaries induced radioactivity with <≈ ms half lives.

References

Aitchison, J., and J. A. C. Brown (1969), *The Lognormal Distribution*, Cambridge Univ. Press, London.

Atwood, W. B., A. A. Abdo, M. Ackermann, et al. (2009), The large area telescope on the Fermi gamma-ray space telescope mission, *ApJ*, *697*, 1071–1102, doi:10.1088/0004-637X/697/2/1071.

Babich, L. P., A. Y. Kudryavtsev, M. L. Kudryavtseva, and I. M. Kutsyk (2007), Terrestrial gamma-ray flashes and neutron pulses from direct simulations of gigantic upward atmospheric discharge, *JETP Letters*, *85*, 483–487.

Carlson, B. E., N. G. Lehtinen, and U. S. Inan (2007), Constraints on terrestrial gamma ray flash production from satellite observation, *Geophys. Res. Lett.*, *34*, L08,809, doi:10.1029/2006GL029229.

Carlson, B. E., N. G. Lehtinen, and U. S. Inan (2009), Observations of terrestrial gamma-ray flash electrons, in *Conf. Proc. 1118, Coupling of Thunderstorms and Lightning Discharges to Near-Earth Space*, edited by N. B. Crosby, T.-Y. Huang, and M. J. Rycroft, pp. 84–91, AIP.

Christian, H. J., R. J. Blakeslee, D. J. Boccippio, W. L. Boeck, D. E. Buechler, K. T. Driscoll, S. J. Goodman, J. M. Hall, W. J. Koshak, D. M. Mach, , and M. F. Stewart (2003), Global frequency and distribution of lightning as observed from space by the optical transient detector, *J. Geophys. Res.*, *208*, 4005, doi:10.1029/2002JD002347.

Cohen, M. B., U. S. Inan, and G. Fishman (2006), Terrestrial gamma ray flashes observed aboard the Compton gamma ray observatory/burst and transient source experiment and elv/vlf radio atmospherics, *J. Geophys. Res.*, *111*, D24,109, doi:10.1029/2005JD006987.

Cohen, M. B., U. S. Inan, R. K. Said, and T. Gjestland (2010), Geolocation of terrestrial gamma-ray flash source lightning, *Geophys. Res. Lett.*, *in press*.

Cummer, S. A., Y. Zhai, W. Hu, D. M. Smith, L. I. Lopez, and M. A. Stanley (2005), Measurements and implications of the relationship between lightning and terrestrial gamma ray flashes, *Geophys. Res. Lett.*, *32*, L08,811, doi:10.1029/2005GL022778.

Dwyer, J. R. (2003), A fundamental limit on electric fields in air, *Geophys. Res. Lett.*, *30*, ASC8.1–ASC8.4, doi:10.1029/2003GL017781.

Dwyer, J. R. (2007), Relativistic breakdown in planetary atmospheres, *Physics of Plasmas*, *14*, 042,901, doi:10.1063/1.2709652.

Dwyer, J. R. (2008), Source mechanisms of terrestrial gamma-ray flashes, *J. Geophys. Res.*, *113*, D10,103, doi:10.1029/2007JD009248.

Dwyer, J. R., and D. M. Smith (2005), A comparison between monte carlo simulations of runaway breakdown and terrestrial gamma-ray flash observations, *Geophys. Res. Lett.*, *32*, L22,804, doi:10.1029/2005GL023848.

Dwyer, J. R., B. W. Grefenstette, and D. M. Smith (2008), High-energy electron beams launched into space by thunderstorms, *Geophys. Res. Lett.*, *35*, L02,815, doi:10.1029/2007GL032430.

Fishman, G. J., P. N. Bhat, R. Mallozzi, J. M. Horack, T. Koshut, C. Kouveliotou, G. N. Pendleton, C. A. Meegan, R. B. Wilson, W. S. Paciesas, S. J. Goodman, and H. J. Christian (1994), Discovery of intense gamma-ray flashes of atmospheric origin, *Science*, *264*, 1313–1316.

Fishman, G. J., M. S. Briggs, V. Connaughton, P. N. Bhat, W. S. Paciesas, A. von Kienlin, C. Wilson-Hodge, R. M. Kippen, R. Preece, and C. A. Meegan (2010), Catalog of terrestrial gamma-ray flashes from the gamma-ray burst monitor on the Fermi observatory, *in preparation*.

Fuschino, F., F. Longo, M. Marisald, et al. (2009), AGILE view of TGFs, in *Conf. Proc. 1118, Coupling of Thunderstorms and Lightning Discharges to Near-Earth Space*, edited by N. B. Crosby, T.-Y. Huang, and M. J. Rycroft, pp. 46–51, AIP.

Grefenstette, B. W., D. M. Smith, J. R. Dwyer, and G. J. Fishman (2008), Time evolution of terrestrial gamma ray flashes, *Geophys. Res. Lett.*, *35*, L06,802, doi:10.1029/2007GL032922.

Grefenstette, B. W., D. M. Smith, B. J. Hazelton, and L. I. Lopez (2009), First RHESSI terrestrial gamma ray flash catalog, *J. Geophys. Res.*, *114*, A02,314, doi:10.1029/2008JA013721.

Gurevich, A. V., G. M. Milikh, and R. Roussel-Dupre (1992), Runaway electron mechanism of air breakdown and preconditioning during a thunderstorm, *Physics Letters A*, *165*, 463–468.

Hazelton, B. J., B. W. Grefenstette, D. M. Smith, J. R. Dwyer, X.-M. Shao, S. A. Cummer, T. Chronis, E. H. Lay, and R. H. Holzworth (2009), Spectral dependence of terrestrial gamma-ray flashes on source distance, *Geophys. Res. Lett.*, *36*, L01,108, doi:10.1029/2008GL035906.

Inan, U. S., and N. G. Lehtinen (2005), Production of terrestrial gamma-ray flashes by an electromagnetic pulse from a lightning return stroke, *Geophys. Res. Lett.*, *32*, L19,818, doi:10.1029/2005GL023702.

Inan, U. S., S. C. Reising, G. J. Fishman, and J. M. Horack (1996), On the association of terrestrial gamma-ray bursts with lightning and implications for sprites, *Geophys. Res. Lett.*, *23*, 1017–1020.

Inan, U. S., M. B. Cohen, R. K. Said, D. M. Smith, and L. I. Lopez (2006), Terrestrial gamma ray flashes and lightning discharges, *Geophys. Res. Lett.*, *33*, L18,802, doi:10.1029/2006GL027085.

Knoll, G. F. (2000), *Radiation Detection and Measurement*, third ed., John Wiley, New York.

Koshut, T. M., W. S. Paciesas, C. Kouveliotou, and J. van Paradijs (1996), Systematic effects on duration measurements of gamma-ray bursts, *ApJ*, *463*, 570–592.

Lay, E. H. (2008), Investigating lightning-to-ionosphere energy coupling based on vlf lightning propagation characterization, Ph.D. thesis, University of Washington.

Lehtinen, N. G., T. F. Bell, and U. S. Inan (1999), Monte carlo simulation of runaway MeV electron breakdown with application to red sprites and terrestrial gamma ray flashes, *J. Geophys. Res.*, *104*, 24,699–24,712.

Lewis, P. A. W., and G. S. Shedler (1978), Simulation of nonhomogeneous poisson processes by thinning, *Tech. Rep. ADA059904*, Naval Postgraduate School, Monterey, CA.

Marisaldi, M., F. Fuschino, and C. Labanti (2009), Detection of terrestrial gamma-ray flashes up to 40 MeV by the AGILE satellite, *J. Geophys. Res.*, *in press*, doi:10.1029/2009JA014502.

Meegan, C. A., G. Lichti, P. N. Bhat, E. Bissaldi, M. S. Briggs, V. Connaughton, R. Diehl, G. Fishman, J. Greiner, A. S. Hoover, A. J. van der Horst, A. von Kienlin, R. M. Kippen, C. Kouveliotou, S. McBreen, W. S. Paciesas, R. Preece, H. Steinle, M. S. Wallace, R. B. Wilson, and C. Wilson-Hodge (2009), The Fermi gamma-ray burst monitor, *ApJ*, *702*, 791–804, doi:10.1088/0004-637X/702/1/791.

Milikh, G. M., P. N. Guzdar, and A. S. Sharma (2005), Gamma ray flashes due to plasma processes in the atmosphere: Role of whistler waves, *J. Geophys. Res.*, *110*, A02,303, doi:10.1029/2004JA010681.

Nemiroff, R. J., J. T. Bonnell, and J. P. Norris (1997), Temporal and spectral characteristics of terrestrial gamma flashes, *J. Geophys. Res.*, *102*, 9659–9665.

Rebinstein, R. Y., and D. P. Kroese (2008), *Simulation and the Monte Carlo Method*, second ed., John Wiley & Sons, Hoboken, New Jersey.

Rodger, C. J., J. B. Brundell, R. H. Holzworth, and E. H. Lay (2009), Growing detection efficiency of the world wide lightning location network, in *Conf. Proc. 1118, Coupling of Thunderstorms and Lightning Discharges to Near-Earth Space*, edited by N. B. Crosby, T.-Y. Huang, and M. J. Rycroft, pp. 15–20, AIP.

Roussel-Dupré, R., and A. V. Gurevich (1996), On runaway breakdown and upward propagating discharges, *J. Geophys. Res.*, *101*, 2297–2311.

Smith, D. M., M. Leventhal, R. Cavallo, N. Gehrels, J. Tueller, and G. Fishman (1996), All-sky search for transient sources near 0.5 MeV with the burst and transient source experiment (batse), *ApJ*, *471*, 783–795.

Smith, D. M., L. I. Lopez, R. P. Lin, and C. P. Barrington-Leigh (2005), Terrestrial gamma-ray flashes observed up to 20 MeV, *Science*, *307*, 1085–1088.

Stanley, M. A., X.-M. Shao, D. M. Smith, L. I. Lopez, M. B. Pongratz, J. D. Harlin, M. Stock, and A. Regan (2006), A link between terrestrial gamma-ray flashes and intracloud lightning discharges, *Geophys. Res. Lett.*, *33*, L06,803, doi: 10.1029/2005GL025537.

Williams, E., R. Boldi, J. Bor, G. Satori, C. Price, E. Greenberg, Y. Takahashi, K. Yamamoto, Y. Matsudo, Y. Hobara, M. Hayakawa, T. Chronis, A. Anagnostou, D. Smith, and L. Lopez (2006), Lightning flashes conducive to the production and escape of gamma radiation to space, *J. Geophys. Res.*, *111*, D16,209, doi:10.1029/2005JD006447.

P. N. Bhat, M. S. Briggs, V. L. Chaplin, V. Connaughton, C. A. Meegan, W. S. Paciesas and R. D. Preece, NSSTC, 320 Sparkman Drive, Huntsville, AL, 35805, USA. (michael.briggs@nasa.gov).

E. Bissaldi and A. von Kienlin, Max-Planck Institut für extraterrestrische Physik, D-85741 Garching, Germany. (azk@mpe.mpg.de)

A. Chekhtman, J. E. Grove, Space Science Division, U. S. Naval Research Laboratory, Washington, D.C., 20375, USA. (eric.grove@nrl.navy.mil)

J. R. Dwyer, Physics and Space Sciences, Florida Institute of Technology, Melbourne, FL 32901, USA. (jdwyer@fit.edu)

G. J. Fishman and C. Wilson-Hodge, Space Science Office, VP62, NASA Marshall Space Flight Center, Huntsville, AL, 35812, USA. (jerry.fishman@nasa.gov)

R. H. Holzworth, Earth and Space Sciences, University of Washington, Seattle, WA 98195, USA. (bobholz@ess.washington.edu)

R. M. Kippen, ISR-1, Los Alamos National Laboratory, Los Alamos, NM 87545, USA. (mkippen@lanl.gov)

D. M. Smith, Dept. of Physics, University of California, Santa Cruz, Santa Cruz, CA 95064, USA. (dsmith@scipp.ucsc.edu)

Table 1. GBM TGFs

TGF	Date	Trigger Time h:min:sec UT	t_{90} start (ms)	t_{90} (ms)	Rise μs	Fall μs	Spacecraft Position East Long.	Latitude	total counts
080807	2008 Aug 7	08:33:24.191042	−10.48	3.08	90	1600	253.01	+15.29	353
080828	2008 Aug 28	10:46:30.271448	−11.54	0.20	50	140	87.72	+23.64	312
081001	2008 Oct 1	09:24:44.927230	−13.00	0.22	90	160	162.67	+10.47	293
081006	2008 Oct 6	19:08:10.745324	−1.00	0.28	60	160	159.70	−12.43	234
081025	2008 Oct 25	16:34:45.557752	−9.82	0.36	80	160	26.87	−1.12	331
081113[a]	2008 Nov 13	07:44:04.238298					7.33	+2.89	
081113a			−1.50	0.18	70	70			132
081113b			−0.14	0.18	7	100			76
081123	2008 Nov 23	20:58:42.331554	−10.32	0.16	30	130	129.88	−15.94	159
081223	2008 Dec 23	01:13:14.665124	−12.46	0.50	140	140	203.33	−16.92	302
090203	2009 Feb 3	08:32:44.380242	−11.44	0.88	380	380	125.87	−16.70	308
090510	2009 May 10	11:57:15.985436	−2.66	2.08	80	1500	24.08	−5.25	237
090522[b]	2009 May 22	04:33:46.890568	−6.80	0.84	230,70	230,70	167.12	−19.10	309
090627[a]	2009 June 27	06:34:48.325250					281.80	+8.10	
090627a			−21.36	0.87	400	400			68
090627b[b]			−12.68	0.52	150,110	150,110			337

[a]TGFs 081113 & 090627 have two emission episodes, denoted "a" and "b" in the table, separated by gaps. The gaps were 1.1 ms long for TGF 081113, and 7.75 ms long for TGF 090627.
[b]TGFs 090522 and episode 090627b consist of two partially overlapping pulses. All values are for the emission episodes (i.e., the sum of the pulses), except that rise and fall times are listed for the individual pulses.

Table 2. GBM TGFs correlated with WWLLN locations

| TGF	time w.r.t trig. time (ms)	Fermi alt. (km)	TGF-WWLLN (ms)	WWLLN Long. (deg)	WWLLN Lat. (deg)	Offset Angle (deg)	Offset Dist. (km)	True Offset (ms)	WWLLN error (μs)
081001	−13.00	546.5	4.40	163.16	11.29	12.4	106.4	2.72	13.2
081113a	−1.50	546.9	0.65	9.01	0.90	31.2	290.4	−1.28	13.8
081113b	−0.14	546.9	2.01	9.01	0.90	31.2	290.4	0.01	13.8
081123	−10.32	558.2	1.79	129.43	−16.18	6.4	55.3	0.02	5.0
090203	−11.44	568.8	−2.28	125.22	−18.91	27.1	256.0	−3.83	11.2

Figure 1. The locations of Fermi at the times of the first 12 TGFs detected by GBM. TGFs which are correlated with WWLLN locations of lightning strokes (i.e., for which a WWLLN location is within 5 ms and 500 km) are shown with red diamonds; the remaining TGFs with blue disks. The GBM detectors are turned off in the cross-hatched region over South America and the South Atlantic to protect them from the increased particle fluxes of the South Atlantic Anomaly (SAA). The dotted orange lines show the 25.6° inclination of Fermi's orbit.
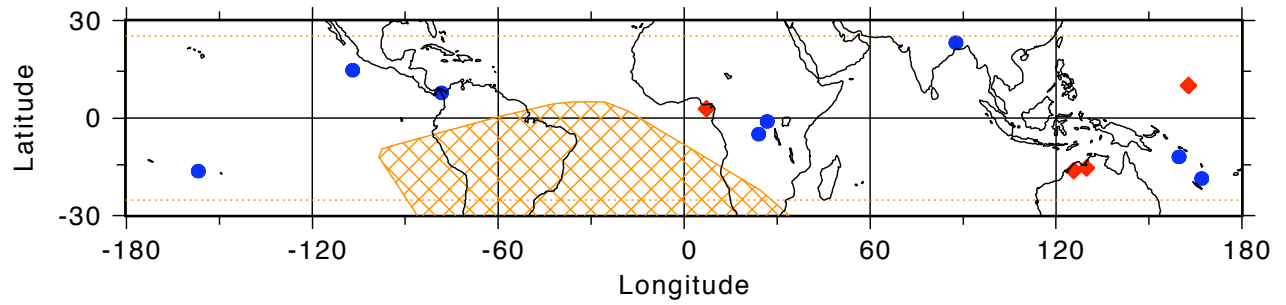
Figure 2. The t_{90} duration measure is calculated by plotting the cumulative counts of the event, as described by *Koshut et al.* [1996]. The bottom panel shows a conventional histogram of TGF 080807, while the top panel shows the cumulative counts. The slanted, dotted lines in the cumulative plot before and after the TGF are linear fits to the nearly constant background rate. The total change in counts due to the TGF is identified. The 5% and 95% points (horizontal dashed lines) in the cumulative curve of increasing counts due to the TGF are identified – the times of these points (vertical dashed lines) are the start and end times of the t_{90} interval. The difference of these two times is t_{90}.
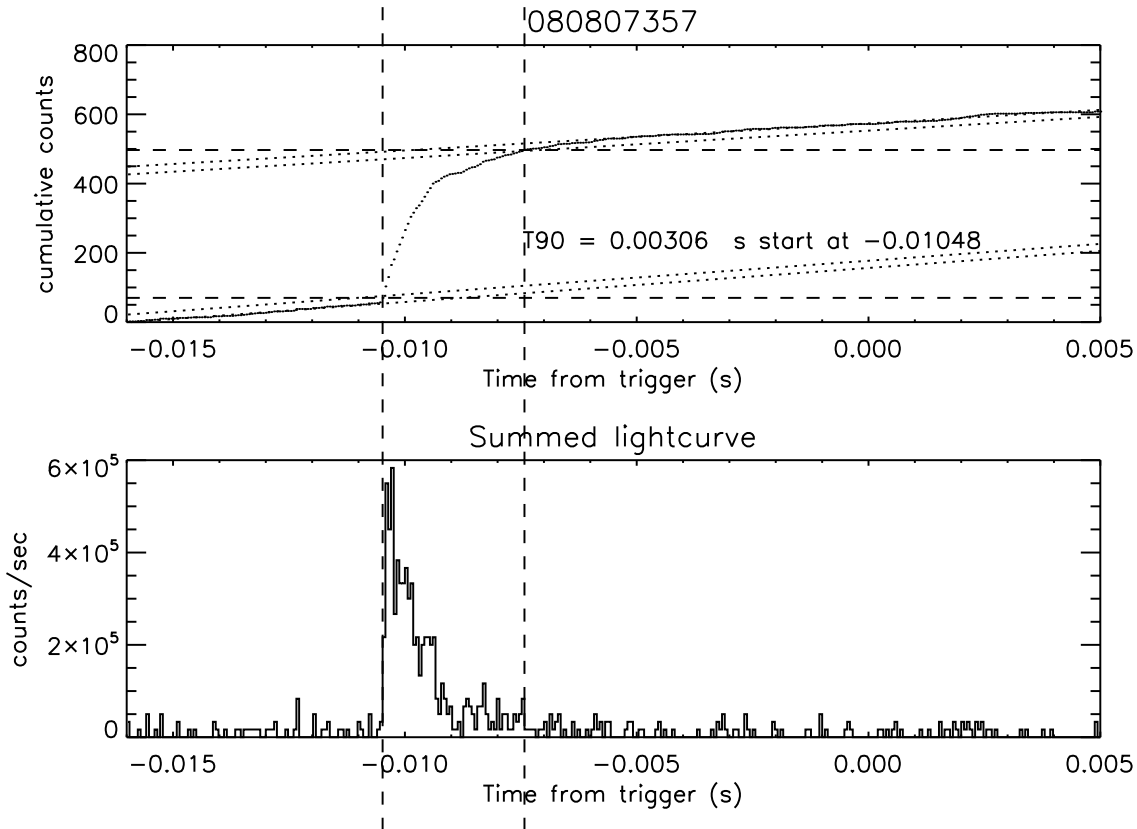
Figure 3. Histograms of the first twelve GBM TGFs (fourteen emission episodes), summed over all 14 GBM detectors (except TGF 080807, which is summed over the 7 detectors on one side of the Spacecraft because there is negligible signal in the detectors on the other side of the Spacecraft), along with curves fit to the data. The curves are fit to the TTE data at the 2 μs intrinsic resolution of the TTE. Pulses consistent with symmetry are fit with Gaussians; asymmetric pulses with the log-normal function. No deadtime corrections are made. The time values on the X-axes are relative to the trigger times, which are listed in Table 1.
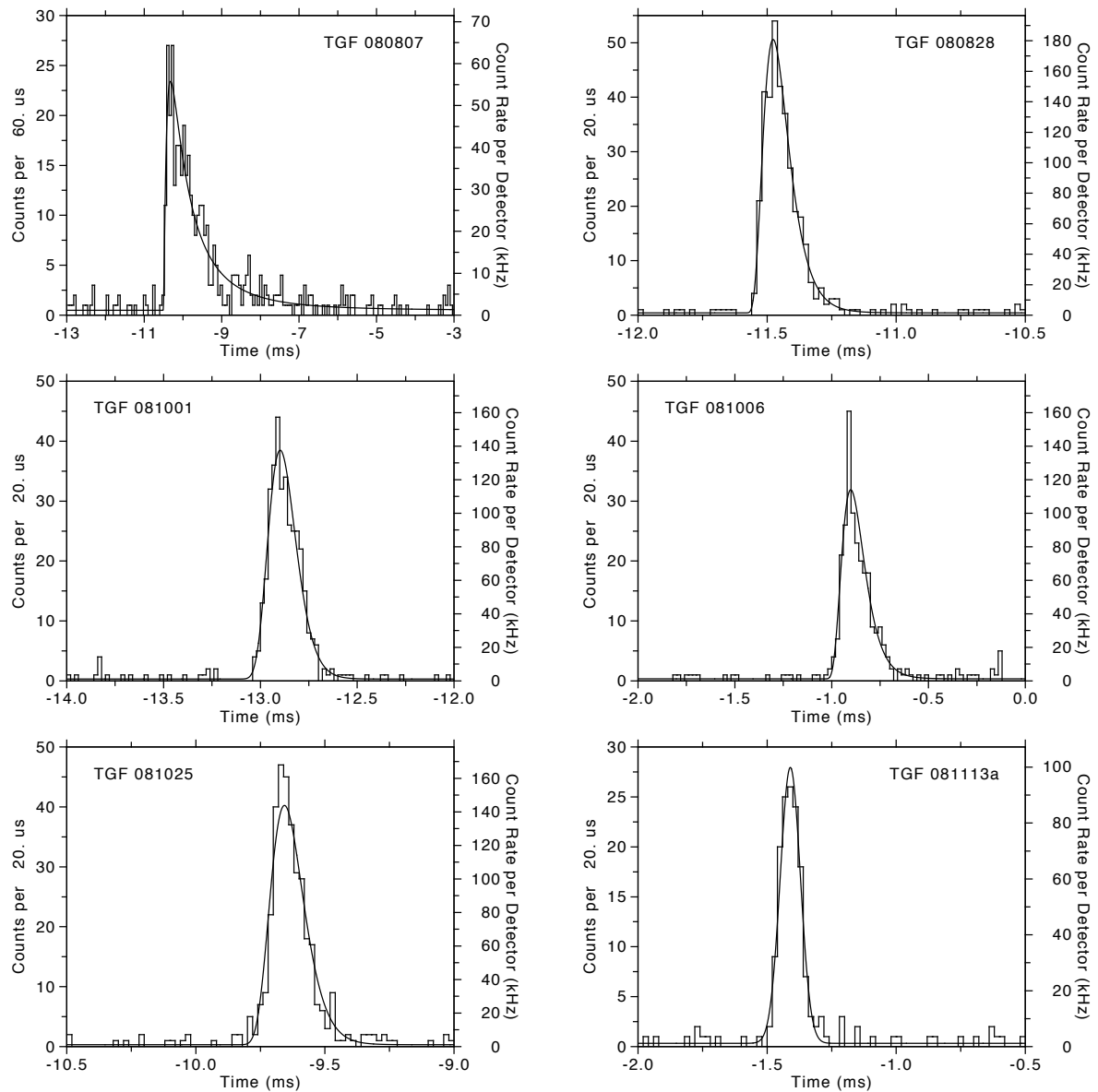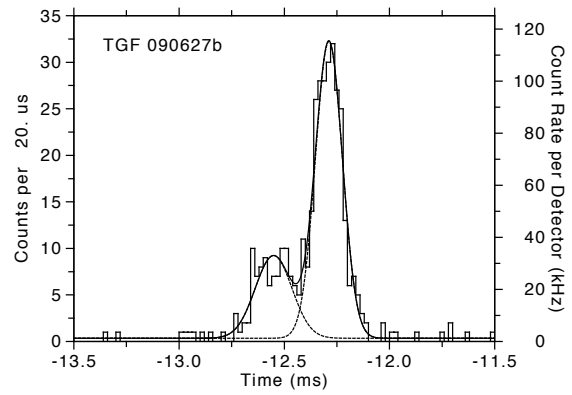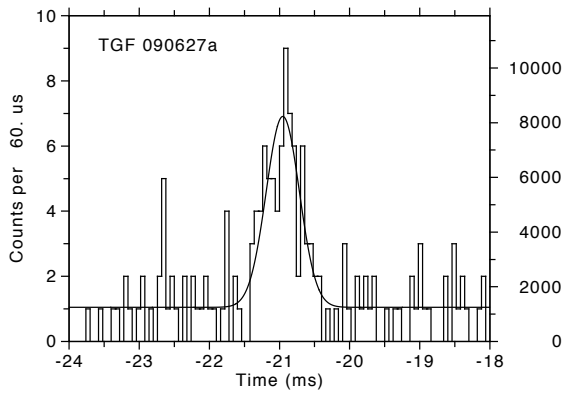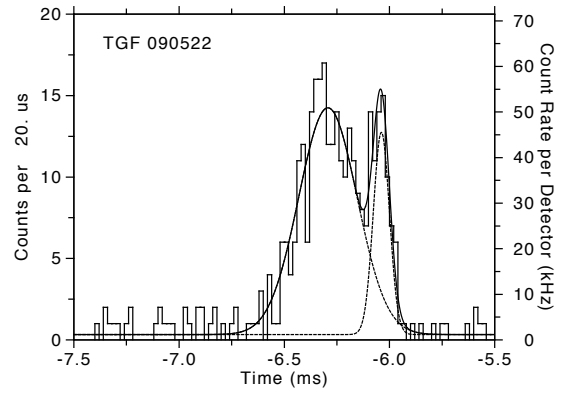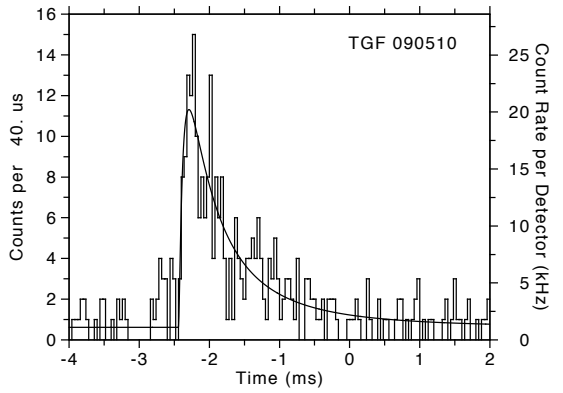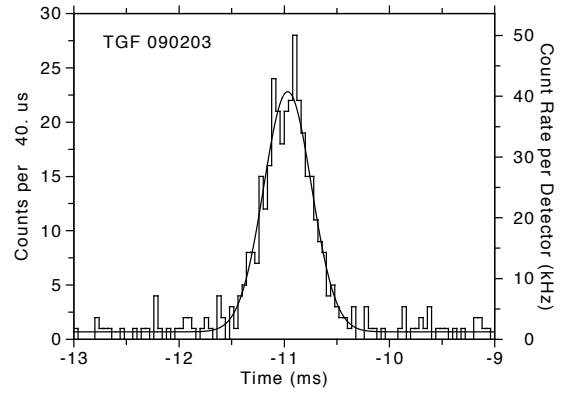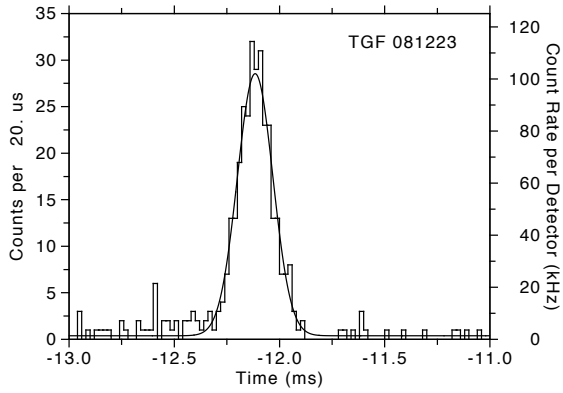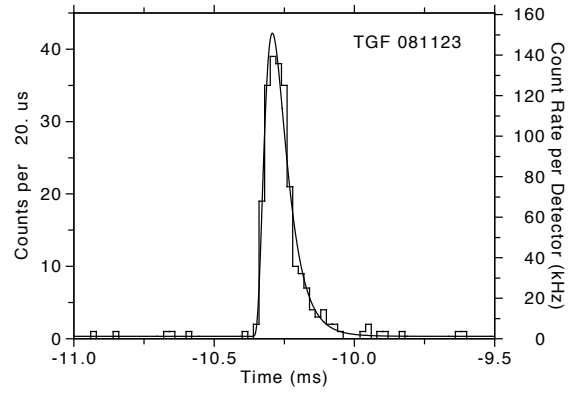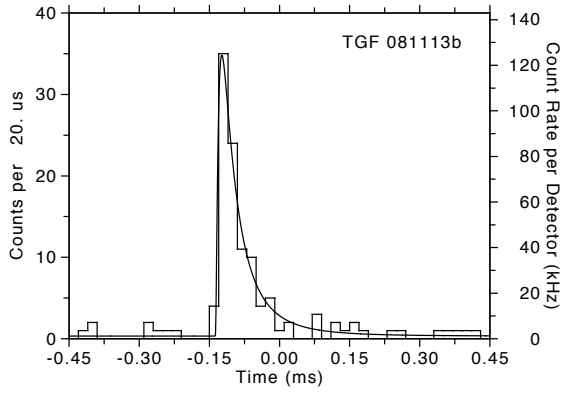
Figure 4. Scatter plots of individual counts from both GBM BGO detectors for two TGFs. Since the BGO detectors have a high probability of absorbing 100% of the energy of a photon, at least up to 10 MeV, in most cases the energy of the count is the energy of the incident photon. Counts detected with BGO 0 are shown with red circles, those from BGO 1 with blue crosses. The time values are relative to the trigger times, which are listed in Table 1. The Y-axes show channel number on the left, with energy indicated on the right. The channels bin the energy of the detected count in a pseudo-logarithmic manner. In addition to the TGF signal, background counts are present. The TGFs clearly stand out above the background. Cosmic rays deposit large amounts of energy and create "overflow" counts, nominally in channel 127 (dotted line). These overflow background counts occur at a higher rate than other high-channel background events. At the time of TGF 081001, for BGO 0, overflow counts occurred only in channel 127, while in BGO 1 overflow counts appeared in channels 124 to 127. The count in channel 125 of BGO 0 coincident with TGF 081001, which is at 38 MeV, is not an overflow count and is most likely from the TGF. A) TGF 080807 B) TGF 081001.
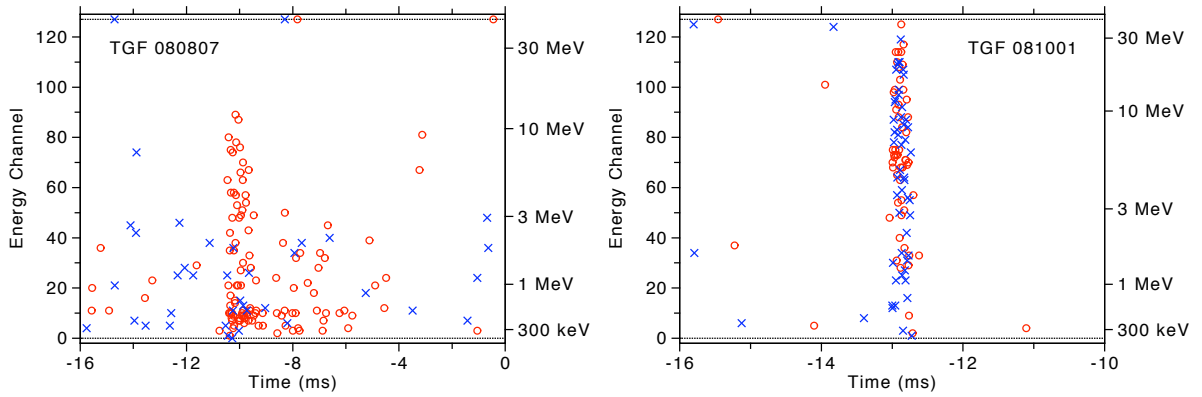
Figure 5. Histograms of the two TGFs in the sample which had separated pulses. The rates are summed from all 14 GBM detectors. Times are relative to the trigger times. Closeup views of the pulses are shown in Fig. 3.
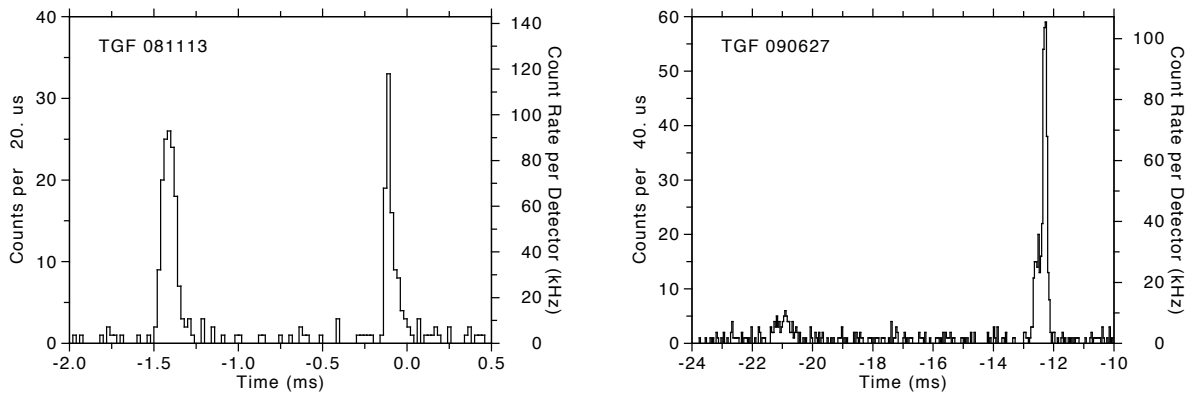
Figure 6. Example alternative fits, in which asymmetric TGF pulses are shown fit both with Log-Normal and Gaussian functions. The Gaussian fits show patterns in the residuals, with the Gaussian function trending below the data before peak of the function, trending above the data after the peak, and below the extended tail. The Log-Normal functions provide better fits.
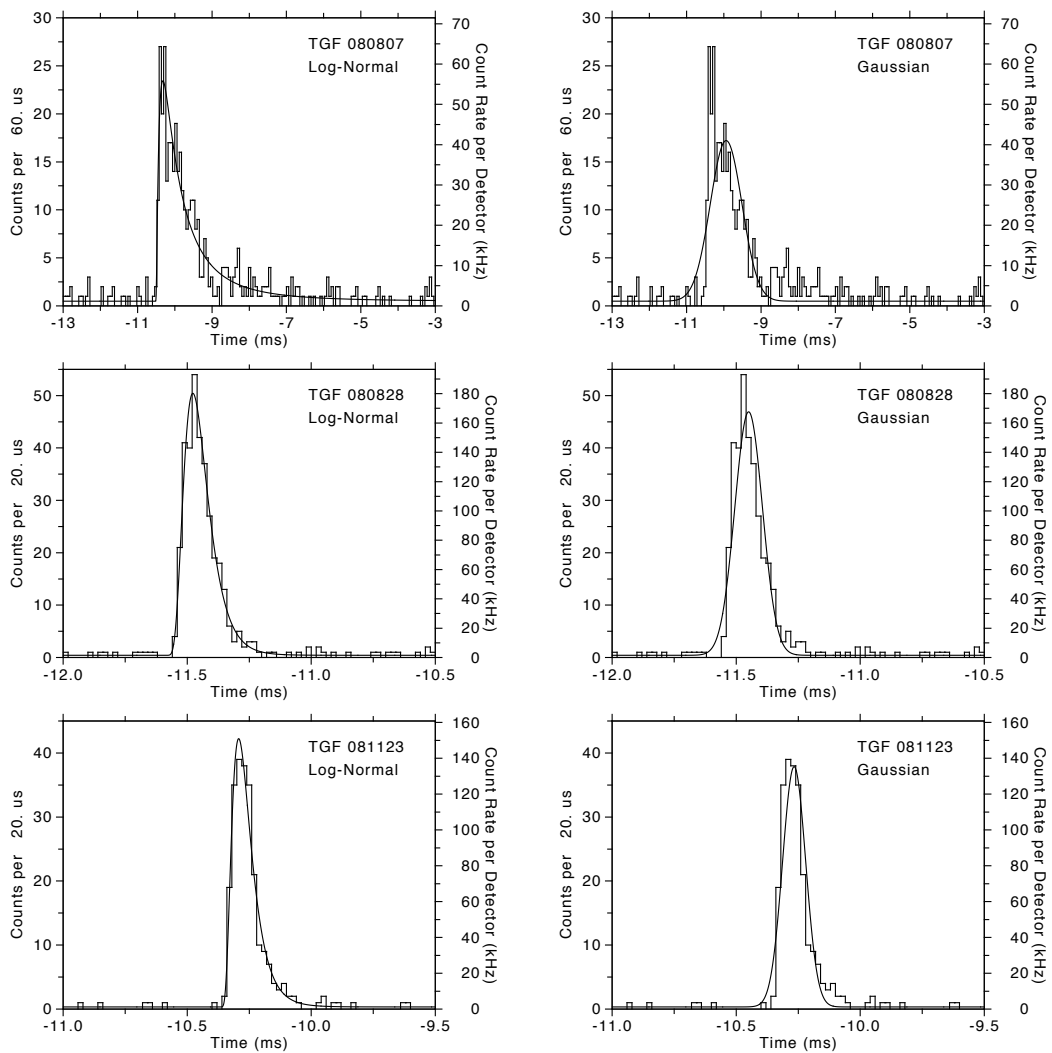
Figure 7. Deadtime analysis of TGF 081001. In each plot, the black histogram shows the counts observed with the two GBM BGO detectors, binned at 40 μs resolution. The blue histograms are the result of one million simulations of photons from the assumed profile, produced pseudo-randomly with Poisson statistics, but without deadtime. The red histograms add to the simulations the effects of deadtime, removing photons that follow within 2.6 μs of an accepted photon. The GBM TTE data were fit at the full 2 μs resolution of the data, optimizing the deadtime-corrected simulation to maximize Poisson likelihood. The binning into histograms is only for display purposes. For the Gaussian fit, the largest difference between the TGF data and the red histogram is about 1.0σ; the deviations for the Log-Normal fit are less. Left: deconvolved assuming a Log-Normal profile. Right: deconvolved assuming a Gaussian profile.
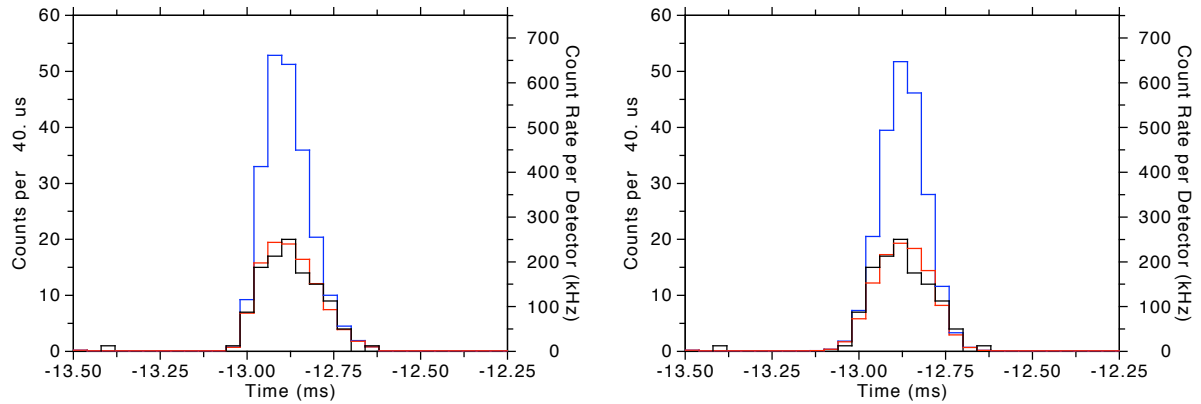
Figure 8. Scatter plots of individual counts from both GBM BGO detectors for the two cosmic ray triggers. A) Trigger 090403.218 begins at −10.706 ms (with respect to the trigger time) with a count in every detector, including counts in channels 128 of both BGO detectors (at the top of the figure), B) Trigger 090408.585 begins at −0.666 ms with a count in every detector, including a count in channel 127 of BGO 0 and channel 128 of BGO 1.